D5.2 – Literature Review of the Benefits and Applications of Very Low Earth Orbits for Earth Observation

Project acronym:	DISCOVERER
Grant Agreement:	737183
Project Duration:	1 January 2017 – 31 March 2021 (51 months)
Version:	1.0
Date:	30/01/2018
WP Leader:	Daniel Garcia-Almiñana
Authors:	Nicholas H. Crisp
	Peter C.E. Roberts
	Sabrina Livadiotti
Due date of deliverable	31/08/2018
Actual submission date	31/08/2018

CHANGE RECORD

Issue	Revision	Date	Modified by	Section/Paragraph modified	Change implemented

TABLE OF CONTENTS

1. Executive Summary

Typical spacecraft operations in LEO are performed in the altitude range above 500km, principally due to the challenges of aerodynamic drag and requirements to provide a meaningful orbital lifetime whilst minimising spacecraft mass and complexity. However, reducing the operational altitude of these spacecraft, particularly for Earth Observation (EO) purposes, can provide a number of benefits which can improve their performance over those operating in higher orbits. This report defines the benefits of using the VLEO range, typically classified as orbits below 450km where atmospheric drag has a significant effect on the platform design, for EO.

Principally for EO applications, a reduction in orbital altitude generally results in a shorter range to the target. For optical imaging systems, including infrared, improved spatial resolution can therefore be achieved with a similar payload. For radar and LiDAR systems, including synthetic-aperture radar, the principal benefit in altitude reduction is to the signal-to-noise ratio, improving the returned image quality. Alternatively, for all system-types, less massive or complex payloads can be considered whilst maintaining similar mission performance. In combination with improvements in radiometric performance and power requirement, the overall size and cost of these systems can be reduced enabling smaller spacecraft with potential savings in cost and development time.

Further benefits of reducing orbital altitude include improved geospatial position accuracy due to the increased proximity to the target and shorter distance over which position and pointing knowledge errors can accumulate, benefits to communications subsystems due to lower downlink power requirements, and improved access-to-orbit as launch vehicles generally have a higher payload performance to lower orbits.

As a result of the increased atmospheric density in these lower orbits, the VLEO range also enables simple compliance with IADC guidelines for deorbit and therefore also demonstrates a lower risk profile for debris collision and resilience to any build-up in the debris population. The radiation environment can also be shown to be more favourable, due in part to the increased atmospheric density.

Finally, the increase in aerodynamic forces, a principal challenge for reducing orbital altitude, can be harnessed to enable novel orbit and attitude control capabilities which are not possible at higher altitudes. These include constellation maintenance and pointing capabilities which can be used to support or improve EO mission performance. Atmosphere-breathing electric propulsion systems can also be considered at these altitudes and used to mitigate the effects of aerodynamic drag, possibly enabling substantial improvements in orbital lifetime even at these significantly lower altitudes.

2. Deliverable report

This deliverable report is principally organised into two sections. The first section describes the individual benefits which are related to performing spacecraft operations in VLEO compared to higher-altitude orbits in LEO. The second section applies these benefits to the Earth Observation (EO) systems and applications identified in the DISCOVERER D2.1 VLEO Aerodynamics Requirements [RD-1] and D5.1 Market Overview [RD-2] reports, providing an overview of the benefits of VLEO to different types of EO missions.

2.1. Benefits of Very Low Earth Orbit

In this section the various benefits of reducing the orbital altitude of Earth observation spacecraft to VLEO (typically below 450km) are identified and discussed. This report builds upon initial work conducted by Virgili Llop et al. [1].

The approach undertaken in this report is to focus on the parameters and system trade-offs which will vary with the orbital altitude of the platform. Where appropriate, the assumption that other necessary parameters do not vary with orbital altitude will be made and that their effect will not be significant on the platform design and operation.

2.1.1. Spatial Resolution

Due to aberrations, diffraction, and distortions, the imaging of a point-source becomes blurred and can be described by a Point-Spread Function (PSF). The angular or spatial resolution describes the ability of an imaging device to distinguish between individual points with small angular separation rather than seeing a single combined or convoluted image. For an imaging system, the theoretical maximum resolution is constrained only by the diffraction of the light or radiated beam through the lens or antenna, described by the Rayleigh criterion which relates the PSF of two neighbouring points [2].

$$\sin\Theta = 1.22\frac{\lambda}{D}$$

where Θ is the angular resolution in radians, λ the wavelength, and D the diameter of the lens or antenna aperture.

The corresponding diffraction limited resolution S_R on the ground can be obtained from the angular resolution by simple trigonometry using the range R and the small-angle approximation:

$$\Theta = \sin^{-1} 1.22\frac{\lambda}{D} = \tan^{-1}\left(\frac{S_R}{R}\right)$$

$$S_R \approx 1.22\frac{\lambda R}{D}$$

The coverage of a spacecraft can be defined by the angular field of regard ψ or total footprint area which is available to a given sensor. These parameters and the associated geometry are described in Figure 1. Alternatively, the instantaneous view of the sensor can be considered, yielding the Field of View (FoV) or sensor footprint area which fall within the angular field of regard.

For a given angular field of regard ψ, the central angle θ from the centre of an assumed circular Earth can be calculated from the orbital altitude via the slant range R and an intermediate angle γ [3].

$$\gamma = \sin^{-1}\frac{r_s \sin\psi}{R_\phi}$$

$$\rho = R_\phi \cos\gamma + r_s \cos\psi$$

$$\theta = \sin^{-1}\left(\frac{R\sin\psi}{R_\phi}\right)$$

The circular footprint area A_F projected on the ground at the nadir can then be approximated using solid angles and is shown to reduce with reducing orbital altitude.

$$A_F = 2\pi(1-\cos\theta)\,R_\phi^2$$

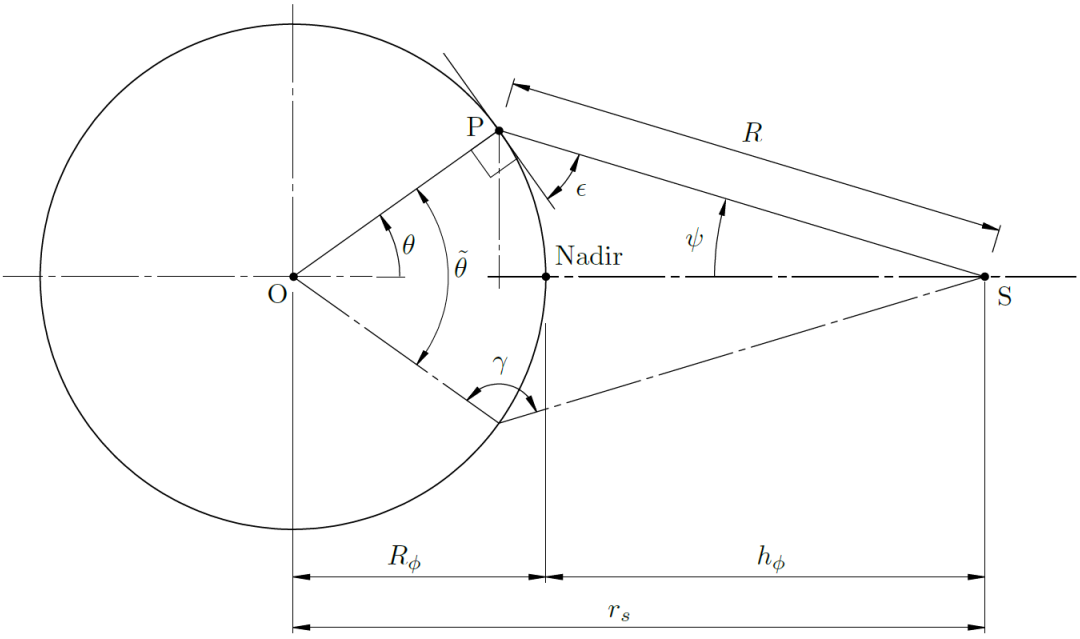

Figure 1 *Sensor footprint geometry. Adapted from Vallado* [3].

As the orbital altitude is reduced the following relationships and general statements regarding the spatial resolution can be made:

i. Spatial resolution increases with reducing altitude for a fixed aperture.
ii. The aperture can be reduced with reducing altitude whilst maintaining spatial resolution.
iii. The available footprint area reduces with reducing altitude for a fixed angular field of regard.

Further constraints on the spatial resolution arise from geometry of the sensor and detecting elements, and any optical or aberrations not accounted for in the system design. However, these parameters are not expected to change with the orbital altitude. Turbulence in the medium through which the signal/light travels to the sensor may also affect the image quality. The system Modulation Transfer Function (MTF), described in Section 2.1.2 seeks to quantify the variation on image quality due to these effects.

The term Ground Sample Distance (GSD) encompasses the first of these constraints and describes the size of the smallest distinguishable element on an acquired optical image.

$$GSD = \frac{xR}{f}$$

where x is the pixel size and f is the focal length to the detector.

2.1.2. Modulation Transfer Function

The Modulation Transfer Function (MTF) can be used to characterise the other conditions which affect the image quality. The MTF effectively represents the variation in contrast or modulation depth (difference between maximum and minimum amplitude) of a sinusoidal image pattern between the object plane and the focal plane. This results from the limited resolution of the system and convolution of neighbouring points which are individually described by a Point Spread Function (PSF) [2].

A PSF is typically used to describe the spread in intensity (ie. blur) of a point-light source which is transmitted through an optical aperture onto an image plane, shown in Figure 2. Due to the interference of the light, a diffraction pattern surrounding the central disk can also often be observed. The properties of the optical lens will further affect the PSF and therefore the clarity or quality of the collected image.

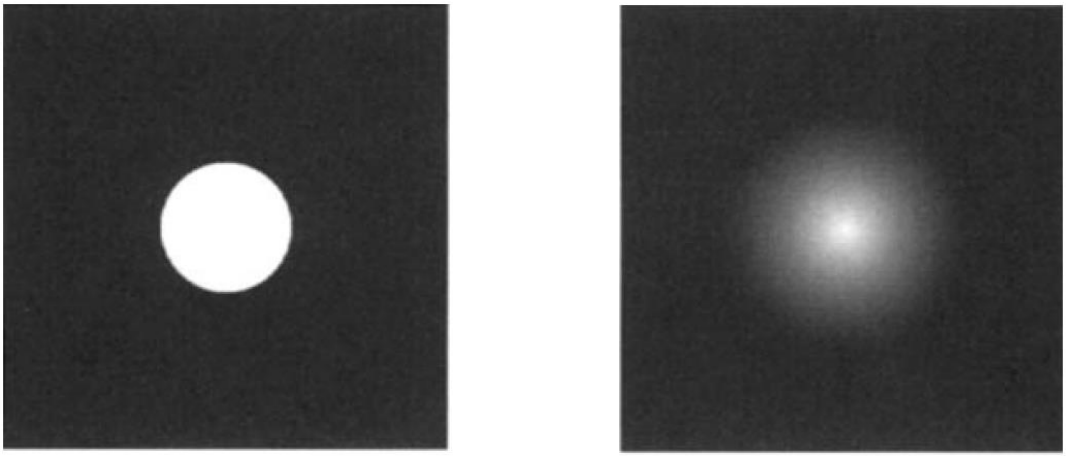

a) b)

Figure 2 *Demonstration of the Point Spread Function: a) input source b) output pattern* [2]

The MTF describes the sensitivity of the imaging chain to the spatial frequency or distribution of imaged objects. As a resulting of the nature of the PSF, the effects of limited spatial resolution become more significant at high spatial frequencies, ie. objects which are spaced more closer together become harder to distinguish from each other. The MTF is therefore often seen as a decreasing function of spatial frequency and can be described as the variation in contrast in an image (shown in Figure 3). The MTF is limited and becomes zero at the spatial cut-off frequency ν_{max} which can be calculated using the aperture diameter D, the focal length f, and the minimum wavelength λ.

$$\nu_{max} = \frac{D}{f\lambda}$$

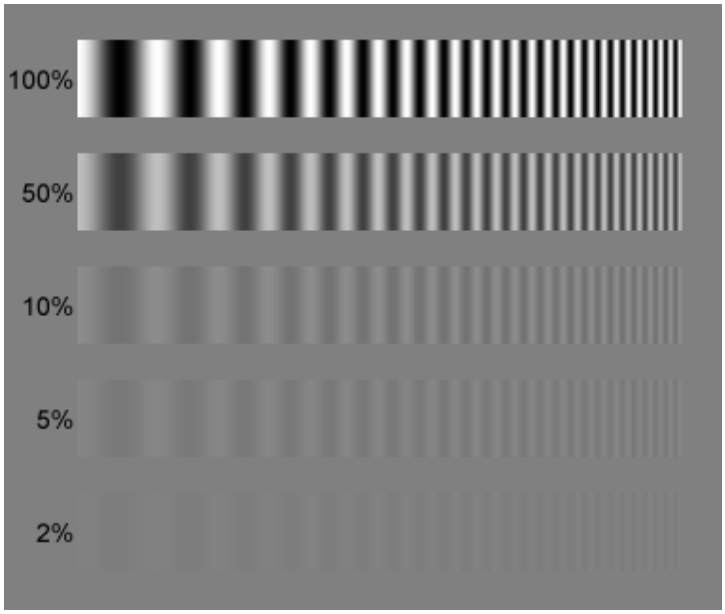

Figure 3 *Effect on image contrast of varying MTF demonstrated using a sine wave pattern* [4]

The total MTF of a system can be determined by multiplication (cascading [2]) of the individual contributing MTFs principally comprised of the following components, which range in value from 0 to 1.

$$MTF_{system} = MTF_{optics} \times MTF_{detector} \times MTF_{motion} \times MTF_{atmosphere} \times MTF_{platform}$$

These contributions and their primary effects will be briefly described individually.

2.1.2.1. Optical Effects

For an optical system with a circular unobstructed aperture and in the absence of aberrations the MTF is simply diffraction limited and can be determined by considering the ratio between the spatial frequency and spatial cut-off frequency [5]:

$$MTF_{optics} = \frac{2}{\pi}\left[\cos^{-1}\left(\frac{\nu}{\nu_{max}}\right) - \frac{\nu}{\nu_{max}}\sqrt{1-\left(\frac{\nu}{\nu_{max}}\right)^2}\right]$$

The absolute MTF is therefore dependent on the aperture diameter, focal length, and wavelength of interest. This MTF will be adversely affected by aberrations and will also vary for more complex optical geometries and lens or mirror configurations. A variation in altitude will therefore not directly affect the optical MTF.

2.1.2.2. Sampling and Detector Effects

The size of the detecting elements in a sensor also present a limit in the spatial frequency and resolution and therefore also contribute to the MTF of the image chain. This effect is principally governed by the size and pitch of the pixels or detector elements and can be expressed in the *across-track* direction for a rectangular detector area as

$$MTF_{detector}(\nu) = \mathcal{F}\left[\frac{1}{|\ell|}\mathrm{rect}\left(\frac{x}{\ell}\right)\right] = \mathrm{sinc}(\ell\nu)$$

where x is the pixel width/length and ℓ is the distance between neighbouring pixel centres.

The detector MTF is therefore improved by increased spacing between detectors but at the expense of signal-to-noise ratio (discussed later) as fewer detection sites will be available. The detector MTF is not directly dependant on the orbital altitude.

2.1.2.3. Motion Effects

The motion of the ground relative to the detector also contributes to the MTF, resulting in blurring of the acquired image due to the sensor integration time [2].

The MTF is derived from a PSF which describes the blur resulting from the distance that the image moves during the sensor integration time, expressed in ground coordinates Y

$$PSF(Y) = \frac{1}{|V_g t|}\mathrm{rect}\left(\frac{Y}{V_g t}\right)$$

where V_g is the ground velocity of the target and t is the integration time of the sensor. The MTF can then be expressed as the Fourier transform of the PSF utilising the scale factor $s = f/R$

$$MTF_{motion}(\nu) = \mathcal{F}\left[\frac{1}{sV_g t}\mathrm{rect}\left(\frac{y}{sV_g t}\right)\right] = \mathrm{sinc}\left(\nu s V_g t\right)$$

Whilst the contribution of orbital altitude or range to the relative velocity and the scale factor in this expression somewhat cancel, the MTF_{motion} is shown to be improved by at greater altitude. However, reduction of the altitude may enable shorter integration times (due to improved signal-to-noise), which may result in an improvement in the motion MTF. The effect of altitude on motion MTF is therefore not considerable.

2.1.2.4. Atmospheric Effects

The contribution to MTF by the atmosphere consists of effects due to turbulence or density fluctuations and scattering or absorption, principally by aerosol particles, which act to introduce random fluctuations in the incoming radiation and result in image blur [2].

The MTF derived from turbulence effects can be described by the refractive index structure coefficient of the medium C_n^2, the path length through the relevant medium R_a, the wavelength of the radiation λ, and the aperture diameter. A parameter μ is used for short-term exposures (otherwise null) and is defined as either $\frac{1}{2}$ or 1 if the subject is in the far or near field [6].

$$MTF_{turbulence}(\nu) = \exp\left(-57.3\nu^{5/3}C_n^2\lambda^{-1/3}R_a\left[1-\mu\left(\frac{\lambda\nu}{D}\right)^{1/3}\right]\right)$$

The MTF due to aerosol presence in the atmosphere is characterised by the effective scattering and absorption coefficients of the particulates S_a and A_a defined differently for spatial frequencies greater and less than the spatial cut-off frequency ν_c [7].

$$MTF_{aerosol}(\nu) = \begin{cases} \exp[-A_a R_a - S_a R_a (\nu/\nu_c)^2], & \nu \leq \nu_c \\ \exp[-(A_a + S_a) R_a], & \nu > \nu_c \end{cases}$$

However, the bulk of the atmosphere (>99.99% by mass) exists below the mesopause (85km) and therefore the entirety of the operable VLEO range. Water vapour and significant aerosol concentrations are also not present in the thermosphere.

The contribution of the atmosphere to MTF is therefore only dependent on the path length to the target through the lower atmospheric regions. However, referring to Figure 1, for a constant angular field of regard, a reduction in orbital altitude results in a greater path length through the atmosphere, and may therefore result in degraded MTF performance.

2.1.2.5. Platform Contributions

The stability of the platform can also contribute to the system MTF as linear motion and dynamic disturbances such as high and low frequency structural vibrations accelerations can cause image blurring [8].

For linear motion of the image plane (the detector), the MTF is dependent on the exposure time t_e and relative velocity of the image plane V

$$MTF_{linear}(\nu) = \mathrm{sinc}(\pi \nu V t_e)$$

High and low frequency vibrations (as sinusoidal motion) are treated separately and determined by comparison of the periodicity of the vibration with respect to the exposure time of the system. The MTF for high frequency sinusoidal motion is dependent on the maximum amplitude of the vibrations A.

$$MTF_{hf}(\nu) = J_0(2\pi \nu A)$$

The corresponding MTF for low frequency vibrations is more complex to determine and is based on the period of the vibration and when during the vibrational motion the exposure is performed. Averaged and statistical methods are often used to determine the MTF for low frequency vibrations.

High-frequency random vibrations, termed jitter can be treated statistically using a Gaussian distribution where σ_R is the RMS displacement [9].

$$MTF_{jitter}(\nu) = \exp(-2\pi^2 \sigma_R^2 \nu)$$

For the bulk of LEO orbits, the platform contributions to MTF will therefore be similar. However, at lower altitudes disturbances related to the atmospheric density (small-scale variations or wind vector) may contribute to the structural vibrations and may result in a degradation in the MTF performance. Due to lack of in-situ studies, these phenomena have not been extensively measured and their effects are therefore poorly characterised.

2.1.2.6. Summary of Altitude Reduction on MTF

The combined MTF of an optical system is generally independent of the altitude at which the platform is operated. However, some effects of variation in altitude can affect the MTF:

- Assuming a fixed optical aperture and detector size, a reduction in altitude may improve the motion MTF performance as the radiometric performance may be improved and the integration time can be reduced.
- For a fixed angular field of regard, a reduction in altitude will increase the path distance through the atmosphere and will therefore experience worse atmospheric MTF performance at the edge of the field of regard in comparison to higher orbits.
- Lower altitude orbits may be associated with additional periodic and non-periodic disturbances related to the atmospheric density and may therefore experience a degradation in MTF performance related to the vibrational response of the platform.

2.1.3.Radiometric Resolution and Performance

The radiometric resolution of a system describes the depth of information which is captured in an image. This radiometric performance is principally dependent on the amount of signal which is received at the detector and the sensitivity of the equipment to the magnitude of the electromagnetic energy to which it is exposed. The radiometric depth is typically measured in number of bits, representing in the number

of different brightness, intensity, or colour levels which can be resolved by the sensor (also known as the dynamic range).

In general, the power or intensity of an emitted signal received at a given distance R (in a vacuum) follows the inverse-square law as it evenly radiated from a point into three-dimensional space.

$$P \propto \frac{1}{R^2}$$

The power of a signal received in orbit is therefore proportional to the distance of the spacecraft to the target and related to the orbital altitude. For active sensor types where a signal is both transmitted and subsequently received by the spacecraft (eg radar) this relationship becomes proportional to the fourth power of the range to the target. A reduction in orbit altitude can therefore significantly increase the power received at the sensor and may allow less sensitive detectors or antennae to be used whilst maintaining similar performance.

The power received by a sensor is also proportional to the collection area. For a circular aperture, for example a telescope, the power is proportional to the square of the diameter D.

$$P \propto D^2$$

As the orbital altitude is reduced the collection aperture can therefore be reduced whilst maintaining a similar radiometric performance.

The signal-to-noise (SNR) ratio received at the sensor or detector is often used to characterise the radiometric performance and can be determined by considering the ratio of signal power received from the source $S(\lambda)$ and the different components of noise $N_x(\lambda)$ as a function of wavelength [10].

$$SNR_{total}(\lambda) = \frac{S_{target}(\lambda)}{\sum N_x(\lambda)}$$

or in units of decibels and generalised to total power

$$SNR_{dB} = 10 \log_{10}\left(\frac{P_{signal}}{P_{noise}}\right)$$

A SNR of greater than 1 is typically necessary to ensure that any signal can be discerned from the background noise levels. However, for precise and accurate measurements or high-quality imagery greater SNRs are often selected.

Alternatively, different noise-equivalent metrics can also be used, for example:

- The noise-equivalent delta in reflectance, ie. the smallest difference in surface reflectance that changes the signal by a value equal to the magnitude of the total noise.
- The noise-equivalent delta in emittance, ie. the smallest difference in surface emittance that changes the signal by a value equal to the magnitude of the total noise.

Sources of noise include those which are related to the sensor and associated electronics and additional components which arise from the contrast between the background and the target and the atmospheric path through which the signal passes. As with the atmospheric contributions MTF, the effect on SNR is principally due to the scattering and adsorption effects of water vapour and other aerosols in the lower strata, leading to signal attenuation. The SNR will therefore be affected by both the total range to the target and the atmospheric path length. The SNR is therefore related to the orbiting altitude and off-nadir angles used by the imaging system.

Radiometric performance is positively affected by a reduction in orbital altitude as the power/signal received improves with reduced range to the target. However, for significant off-nadir viewing angles the SNR performance may degrade as the range to target through the lower atmosphere increases.

These relationships are also consistent with the trends identified for diffraction limited resolution. As the orbital altitude is reduced the aperture diameter can be made smaller whilst broadly maintaining the same radiometric performance and spatial resolution. Alternatively, if the same aperture diameter is maintained the radiometric performance and spatial resolution will be improved with reducing altitude.

2.1.4. Temporal Resolution

Revisit time, defined as the time for a satellite to acquire successive viewings of target locations on the Earth's surface can highly influence satellite constellation design, configuration, performance and technology selection [11]. Low Maximum Revisit Time (MRT) is generally desired along with global coverage (or between prescribed latitude bands) for most Earth observation and remote sensing applications.

The selection of a repeating ground-track orbit is not strictly required for EO missions, but it represents a critical requirement when regular passes over specific locations are fundamental for achieving the mission objectives. Short-period repeating ground-tracks are more easily achievable for higher LEO altitudes (600-1000 km), where external perturbations typically have less effect on the orbital dynamics. In the VLEO altitude range, the residual atmospheric interaction with the satellite's external surfaces gradually causes the orbit to decay, thus making repeating ground-tracks only achievable when aerodynamic compensation devices or aerodynamic control techniques are employed [12].

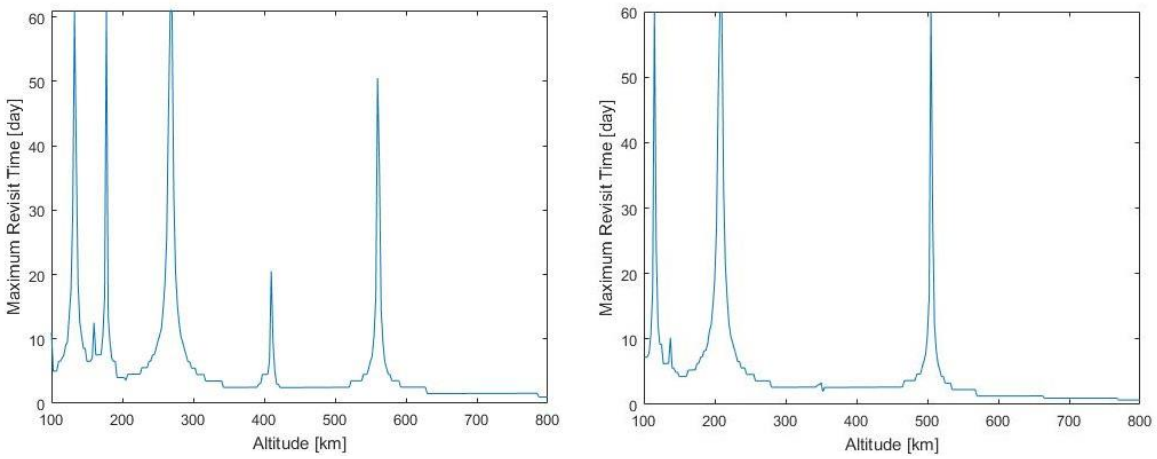

Figure 4 Left: *MRT for varying SSO altitude. FoR and target latitude are fixed (ψ=45° and ϕ=40°).* ***Right:*** *MRT for varying non-SSO altitude. FoR, target latitude and orbit inclination are fixed (ψ=45°, ϕ=40° and i=60°).*

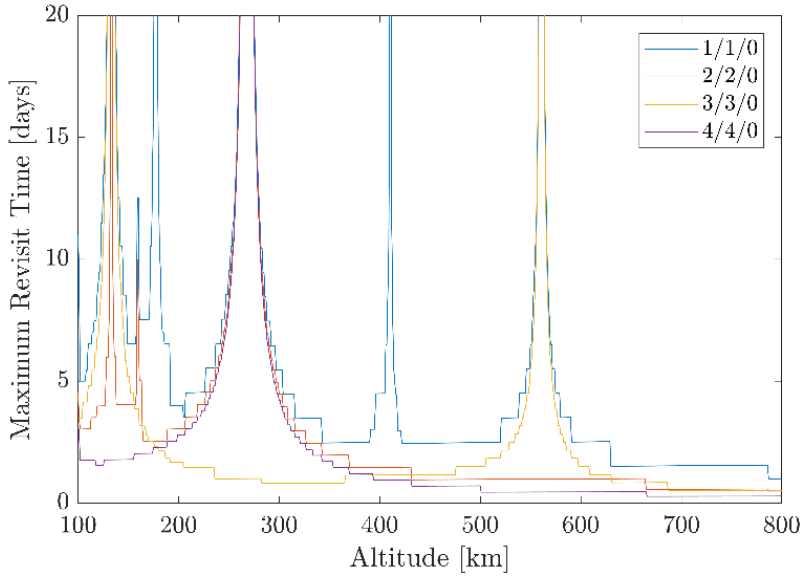

Figure 5 *MRT computation for varying Sun-synchronous orbit altitude and constellation configuration for a target latitude of 40° and sensor boresight half-cone angle of 45°.*

Figure 4 (Left) show how MRT varies according to altitude for circular SSOs, when the Field of Regard (FoR) angle ψ is equal to 45° and the target latitude ϕ is 40°. Some altitude ranges provide poor temporal resolution, and for this reason should be avoided. The performance of these altitudes typically results from resonance of the orbital period leading to incomplete coverage of all latitudes, or very long repeat ground-track patterns.

However, for the VLEO range, close to optimal MRT is still achievable for certain altitude windows, which thus represent a restriction on the usable altitudes in this range which the satellite can operate in. Currently, the majority of the EO missions are launched into SSO for the advantageous illumination conditions these orbits offer. However, it is worth mentioning that the results obtained for non-SSOs demonstrate a meaningful temporal resolution improvement for VLEO, indicated in Figure 4 (Right).

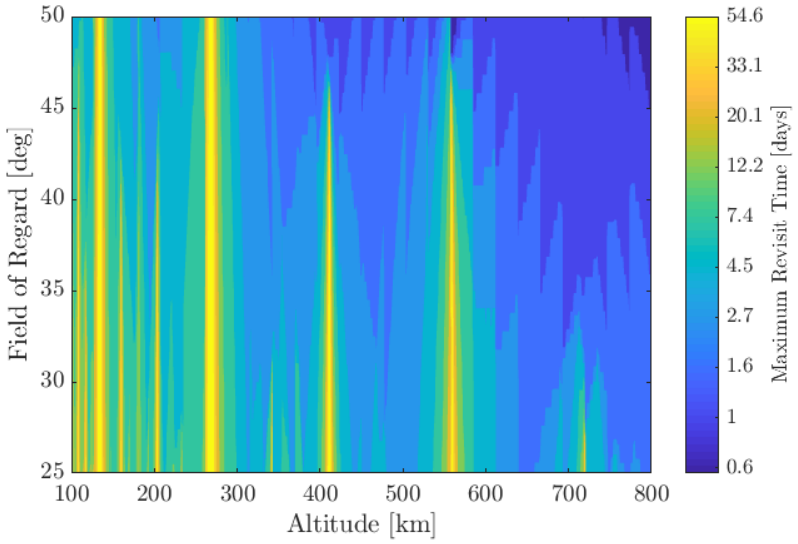

Figure 6 *Contour plot of MRT for varying Sun-synchronous orbit altitude and sensor boresight half-cone angle for a single satellite and target latitude of 40°.*

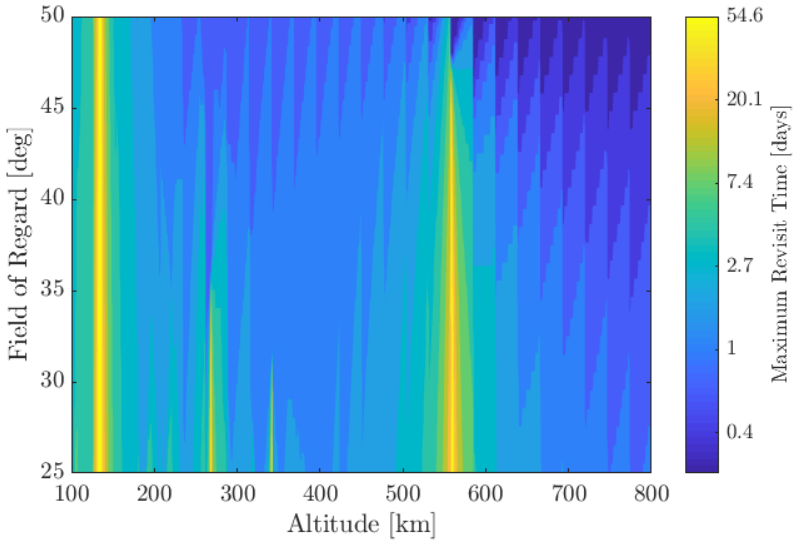

Figure 7 *Contour plot of MRT for varying Sun-synchronous orbit altitude and sensor boresight half-cone angle for a 3/3/0 constellation and target latitude of 40°.*

Temporal resolution can introduce some constraints on the altitude windows in which LEO satellite constellations can be operated. The low MRT achievable for the range 600-800 km generally makes these altitude windows suitable for most EO missions. For certain ranges, small changes in altitude can result in significant variation in temporal resolution performance. However, it is interesting to notice how SSO constellations consisting of an odd number of planes, each occupied by a single satellite, can provide significant improvement for certain lower altitude windows, granting comparable performance in terms of temporal resolution to higher altitudes. In Figure 6 and Figure 7 this is demonstrated by the low MRT for a Walker Delta configuration[1] of 3/3/0 over the altitude range of 200 to 350km.

[1] Typically described as **i:t/p/f** where **i** is the inclination, **t** the total number of satellites, **p** the number of planes, and **f** the relative spacing between satellites in adjacent planes.

2.1.5.Geospatial Position Accuracy

The error between the reported/recorded and actual location of an acquired image or other Earth Observation measurement is generally referred to as the geospatial or geometric position accuracy. The principal contributors to errors in geospatial position are the uncertainty in the spacecraft position and attitude, and errors associated with the alignment and calibration of the observing sensors. A distributed set of Ground Control Points (GCPs) are often used to provide correction to acquired data and imagery, improving the geospatial position accuracy.

The principal geospatial errors are associated with the satellite position (in-track, cross-track, and radial), and pointing (elevation/nadir, and azimuthal). Additional errors also arise from the uncertainty in the altitude of the observed target, and uncertainty in the rotational position of the Earth due to clock errors. These errors are described by the following equations [13] where h_T is the altitude of the target on the Earth's surface.

$$E_{azimuth} = \Delta\phi \, R \sin\eta$$

$$E_{elevation} = \Delta\eta \, \frac{R}{\sin\varepsilon}$$

$$E_{in-track} = \Delta I \, \frac{R_\phi + h_T}{r_s}\sqrt{1-(\sin\lambda\sin\phi)^2}$$

$$E_{cross-track} = \Delta C \, \frac{R_\phi + h_T}{r_s}\sqrt{1-(\sin\lambda\cos\phi)^2}$$

$$E_{radial} = \Delta(r_s) \, \frac{\sin\eta}{\sin\varepsilon}$$

$$E_{altitude} = \Delta(R_\phi + h_T)\frac{1}{\tan\varepsilon}$$

$$E_{clock} = \Delta T \omega_E \cos\varphi$$

The geospatial position errors due to error in the satellite position (in-track, cross-track, and radial) show an inversely proportional relationship to the orbital altitude, whilst the corresponding errors associated with the satellite attitude (azimuth and elevation) are proportional to the range to the target.

The relationship between these different error sources and the resulting geospatial position accuracy with reducing orbital altitude are shown in Figure 8. The trends in errors associated with the pointing/attitude errors particularly demonstrate that the geospatial position accuracy generally improves with reducing orbital altitude.

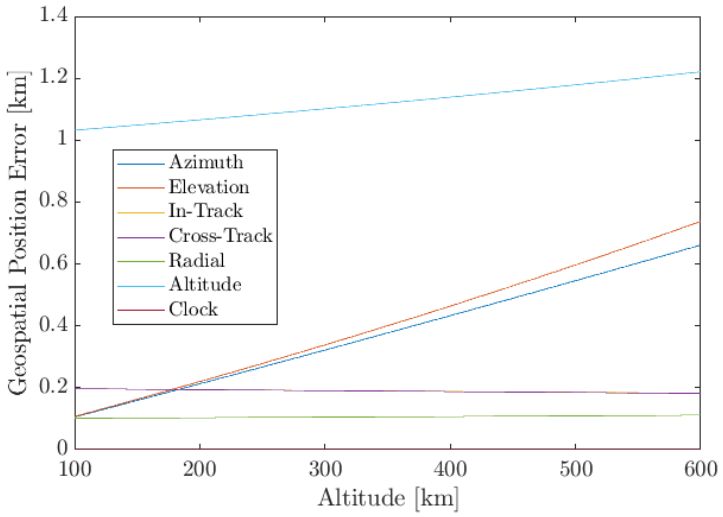

Figure 8 *Geospatial position error for an equatorial ground target with varying altitude at an off-nadir pointing angle of 45° (Error sources: $\Delta\phi = 0.06°$, $\Delta\eta = 0.03°$, $\Delta I = \Delta C = 0.2km$, $\Delta R_s = 0.1km$, $\Delta R_T = 1km$, $\Delta T = 0.5s$)*

The errors associated with the attitude and position of the spacecraft are also based on the available sensors and orbit/attitude determination capabilities. Factors which can affect the accuracy of these sensors may also subsequently affect the geospatial position accuracy of acquired imagery and data.

For example, evidence of ionospheric interference of GPS devices in low Earth orbits resulting in tracking losses has been observed, particularly at high-latitudes and periods of high solar activity [14].

2.1.6.Communication and Link Budget

The communications performance of a space system is dependent on the location of available ground stations and in-orbit networks, the orbital parameters, and the subsystem and hardware selection. Variation in the orbit altitude can therefore have an impact on the overall communications performance which can be achieved in orbit.

The radiometric performance of data communications (receiving and transmitting data) is broadly similar to the relationships described in Section 2.1.2.6. Principally, the free-space loss reduces with the shorter range to the target groundstation (inverse-square law [13]) and the signal-to-noise ratio therefore improves for an antenna of the same size and effective isentropic radiated power ($EIRP$). The radiated power P_r received at the range R is dependent on the receiving antenna diameter D and the antenna efficiency η.

$$P_r = EIRP \cdot \frac{L_a D^2 \eta}{16R^2}$$

The transmission path loss L_a, including absorption due to the ionosphere, atmosphere, and rain, is dependent on range and therefore the off-nadir angle. Thus, for lower altitude orbits, a constraint on elevation angle to ensure a reliable communication link may become a limiting factor [15]. In the calculation of SNR, further sources of noise should also be considered including antenna, cosmic background, Earth (natural and man-made), and solar sources [16].

In addition, the velocity increase with reducing orbital altitude may also adversely affect the available duration for communication with a given ground station, reducing the volume of data which can be transferred.

Finally, the frequency of passes within range of the available ground stations should be considered for different orbital altitudes as per the discussion in Section 2.1.4. If fewer passes of available ground stations are performed each day for a lower altitude orbit, the total volume of data which can be transmitted or received may be constrained despite the improvement in radiometric performance.

2.1.7. Deorbit Requirements

The Inter-Agency Space Debris Coordination Committee (IADC) guidelines define LEO (up to 2000km) as a protected region of Earth orbit and outline that any spacecraft which operating in this region should either be deorbited after the completion of operations or have a maximum lifetime of less than 25 years [17]. These recommendations are also incorporated into space agency requirements and policy (NASA, ESA) and an ISO Standard (24113:2011 Space systems – Space debris mission requirements). However, whilst these guidelines and associated standard are not technically law or regulation, they are often used by national agencies and governing authorities when considering whether to grant launch licenses and must therefore be satisfied in most cases to successfully gain access-to-orbit.

The post-mission orbital lifetime of a spacecraft in LEO can extend to many hundreds or thousands of years depending on the orbital parameters and physical properties. However, as orbital altitude is reduced the residual atmosphere of the Earth becomes denser the lifetime quickly decreases. Lower Earth orbits are therefore more likely to directly comply with the deorbit requirements.

Estimation of orbital lifetime is a difficult process due to the uncertain nature of the thermospheric density. Whilst atmospheric density models are openly available, these can have significant uncertainties, bias, and errors which will affect the estimated lifetime. These models are also highly dependent on the predicted solar cycle which is a principal driver of the variation in atmospheric density. Models and forecasts for the solar cycle are also available, but often later found to be inaccurate and unable predict the correct trend in solar radio flux. Orbital lifetime prediction methods can also vary significantly in fidelity depending on the type of propagation performed (analytical vs numerical), scope of the perturbations included, and the input data used.

However, by using simple analytical or semi-analytical methods the variation in orbital lifetime for spacecraft in LEO for different altitudes can be illustrated. Figure 9 shows this significant variation in orbital lifetime which occurs with altitude, solar flux input to the atmosphere, and physical satellite characteristics (ballistic coefficient or mass to area ratio). The use of a ballistic coefficient includes the contribution of a drag coefficient (a value of 2.2 is used here). However, if significantly lower coefficients

of drag can be produced, through development of low drag materials and geometries, the lifetime of spacecraft in all orbits can be increased.

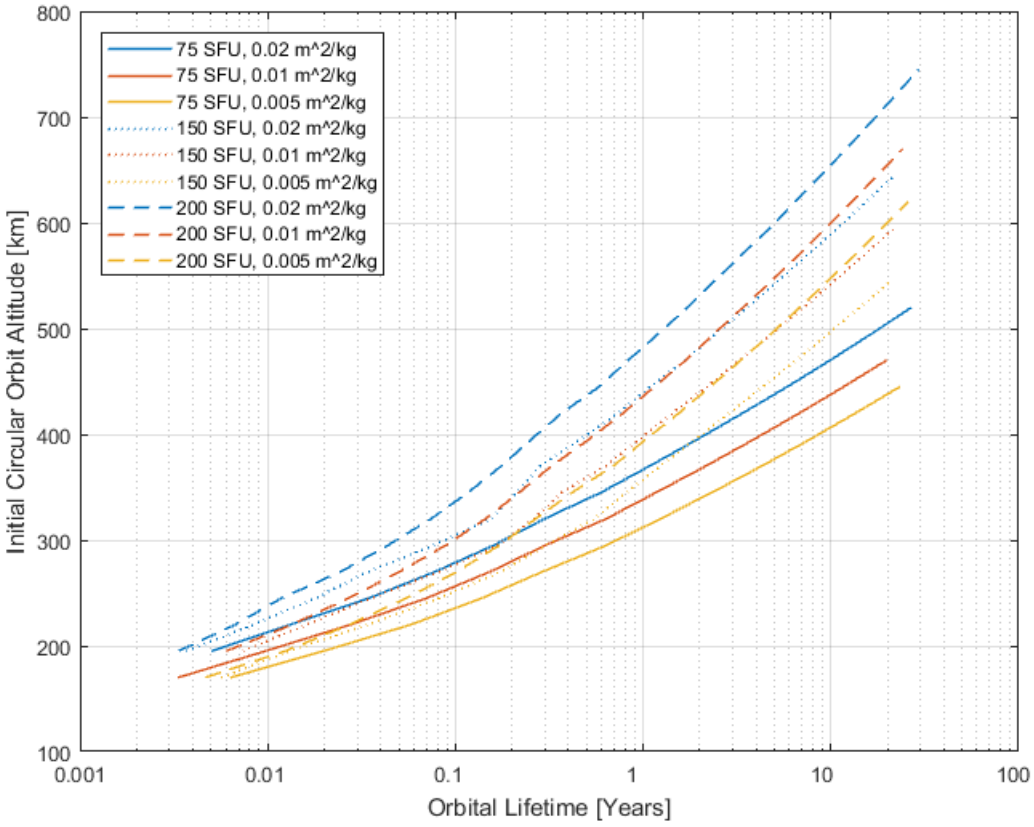

Figure 9 *Orbital lifetime for varying ballistic coefficient and solar radio flux conditions. Generated using semi-analytical propagation based on SALT* [18] *and NRLMSISE-00* [19] *atmosphere model.*

The results presented broadly demonstrate that any satellite operating in a VLEO orbit (below 450km) will have a post-mission lifetime of less than 25 years, regardless of the solar environment and satellite size and mass. Oltrogge and Chao [20] present a different approach for lifetime analysis which utilises a random draw method for the solar flux, but similarly show that orbits below 500km generally have a lifetime of less than 25 years.

VLEO orbits are therefore generally compliant with the IADC guidelines and corresponding licencing requirements. Furthermore, this compliance is not conditional on any additional deorbit hardware or propulsion system which can add complexity, cost, and system mass.

2.1.8. Debris Collision Risk Resilience

The debris environment which exists in Earth orbit is predominantly a result of the exploration and operational activities which have occurred since the beginning of human involvement in space. In addition to naturally occurring micrometeoroids the objects which persist in orbit principally include post-mission and failed spacecraft, launch vehicle upper stages, deployment and other mission-related items, and surface degradation and propulsion products amongst other miscellaneous objects [21]. Explosions, collisions, and break-up or fragmentation events within this population have further increased the number and dispersion of these objects in the orbital environment.

In LEO, the residual atmospheric environment causes these objects to decay, eventually causing re-entry. However, as the atmospheric density reduces roughly exponentially with altitude, the rate of decay from high and med-LEO is slow, and the lifetime of debris can often exceed the mission lifetime of many spacecraft. However, in VLEO the atmospheric density is higher and any debris which is generated in or enters this regime from higher orbits will therefore decay at a faster rate.

Prediction of the future space debris environment can be generated using ESA's MASTER (Meteroid and Space Debris Terrestrial Environment Reference) tool [22]. This tool provides the capability to predict the spatial density or flux of known debris sources (greater than 1µm) against a target spacecraft surface/volume. The current prediction of future debris spatial density, assuming a business-as-usual

case with no additional debris mitigation, is shown for the range of LEO orbits in Figure 10 for the period 2020 to 2055. The average spatial density over this period is calculated for each altitude and shown in Figure 11. In both cases, the VLEO range (<500km) is clearly shown to have a lower spatial density profile than higher LEO orbits and appears to be resilient to the debris build up which is predicted for the 700-1000km range towards 2055.

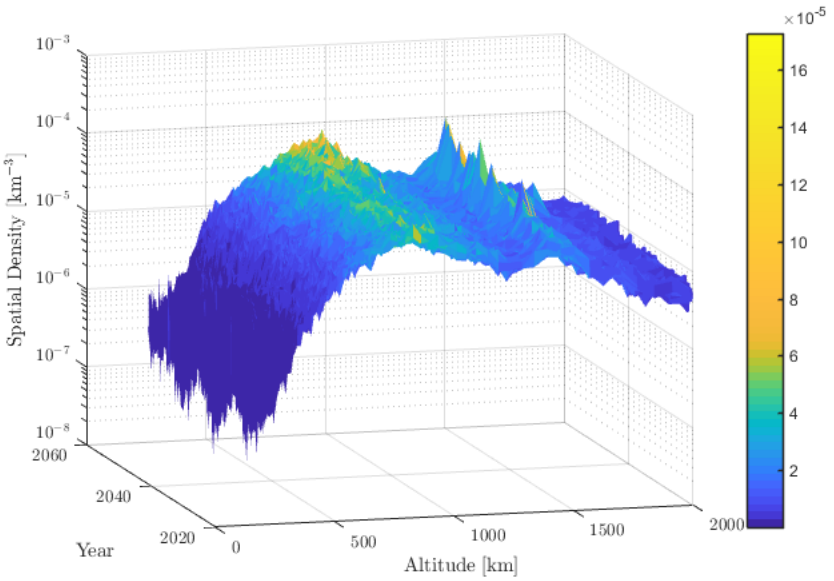

Figure 10 *Simulated LEO debris population (spatial density) over the period 2020 to 2055 based on a "Business-as-usual" scenario with no debris mitigation. Generated using the ESA MASTER-2009 tool.*

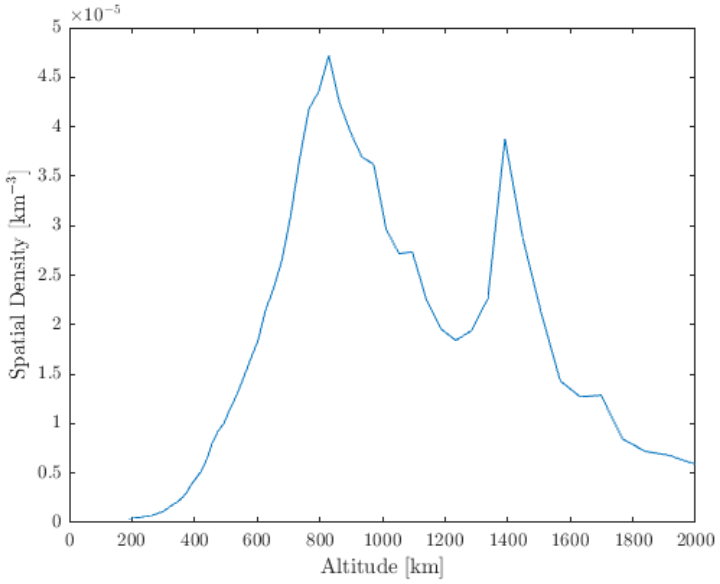

Figure 11 *Spatial density for LEO altitudes averaged over the period 2020 to 2055.*

The assessment of collision risk in orbit includes both the probability and potential consequence and is a combination of the spacecraft composition and geometry, the debris environment, and the relative collision velocity [23]. Using the spatial density profiles presented to describe the probability of a collision, the VLEO range is shown to be able to remain at a lower relative risk than other orbits which may become more polluted. Similarly, the risk to VLEO in the case of a Kessler syndrome type cascade event will remain relatively low as any debris will quickly decay and deorbit. However, the risk profile will still increase somewhat in this scenario due to the increased flux of debris which transits through the VLEO range.

2.1.9. Radiation Environment

The radiation environment which a spacecraft is subjected to in LEO consists of a combination of energetic particles trapped by the Earth's magnetic field, solar flares, and galactic cosmic rays [24]. These sources of radiation can interact with the sensitive components of spacecraft subsystems causing both long-term and single-event effects which can have significant detrimental effect on a spacecraft mission. Radiation-hardened electronic components or fault-resilient software systems are therefore typically employed at significant additional cost. Radiation-shielding can also be employed to reduce the radiation dosage which internal components are exposed to [13].

The radiation environment can also affect the performance and longevity of materials (eg. polymer embrittlement) used on a spacecraft [25]. For long-duration missions, alternative material choices or design redundancy may therefore be required to ensure structural integrity, possibly increasing system mass and cost.

The radiation environment in Earth orbit is characterised by the presence of the magnetosphere and the Van Allen radiation belts [16]. The exposure due to the trapped-radiation in the Van Allen belts is known to vary broadly with the solar cycle and can be modelled by NASA's AP-8 and AE-8 models for proton and election content respectively at either the maximum or minimum solar conditions.

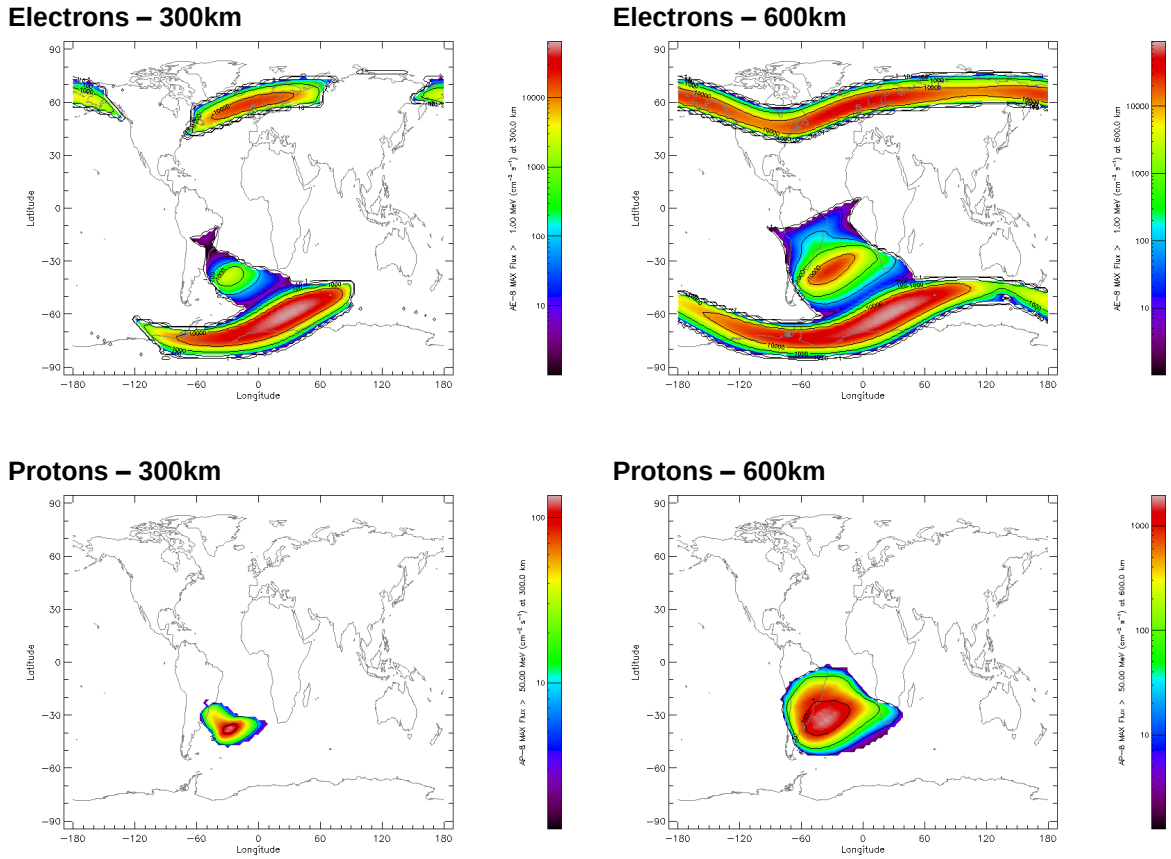

Figure 12 *Proton (AP-8 model) and electron (AE-8 model) flux at 300km and 600km altitude at solar maximum conditions. Generated using ESA SPENVIS.*

In the LEO range, the distribution of protons and electrons of varying energy level can be plotted using these models via SPENVIS [26], shown in Figure 12. The peak radiation flux can be shown to reduce considerably between 600km and 300km, as a result of the additional atmospheric density [27], thus demonstrating a benefit in operating at a lower orbital altitude.

With increasing interest and use of COTS (Commercial Off-The-Shelf) components [28–31] without radiation-hardening, a reduction in radiation exposure at lower altitudes may enable longer duration missions utilising these components as the lifetime dosage reduces correspondingly. Alternatively, even cheaper consumer components may be able to be successfully used in VLEO, further decreasing mission costs and system development time.

2.1.10. Access to Orbit

The payload performance or launch mass of an orbital launch vehicle generally increases with reducing altitude, principally due to lower gravity losses and shorter flight-times and therefore reduced fuel requirements. A comparison of the SSO launch capability of different vehicles is shown in Figure 13, illustrating the increase in launch performance which can be achieved for lower altitude insertion orbits.

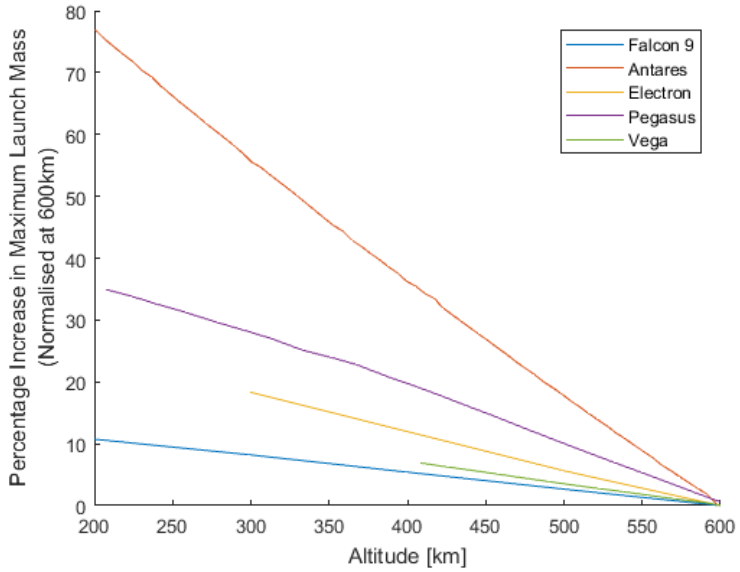

Figure 13 *Variation in SSO launch capability with decreasing altitude for different launch vehicles* [32–36]

For different vehicles, the improvement in launch capability from 600km to 300km insertion ranges from approximately 10% to over 50%, demonstrating potential for a significant increase in mass which can be launched to lower altitude orbits.

A greater number of satellites can therefore be delivered per launch to orbit for no additional cost. Alternatively, for shared launch services, the unit cost (cost per kg or per satellite of a given mass) can be decreased, improving the accessibility of VLEO missions.

Finally, as each vehicle has a greater payload capability to lower altitude orbits the number of vehicles which can launch a given spacecraft may be increased, thus increasing competition and providing alternative options in the case of potential launch delays.

2.1.11. Aerodynamic Forces

In LEO, the interaction between the residual gas particles and the external surfaces of a spacecraft results in the generation of aerodynamic forces and torques. The principal force generated is drag, which acts to cause orbital decay and eventually deorbit. However, out-of-plane forces can also be generated and can contribute to orbital manoeuvring. These forces, in combination with the spacecraft geometry, can also be used to generate torques and used to modify the spacecraft stability and provide attitude control.

A range of different attitude and orbit control methods using these aerodynamic forces and toques have been described and proposed in the literature. A comprehensive review of these methods is provided in the DISCOVERER D2.1 VLEO Aerodynamics Requirements report [RD-1].

In brief, orbit control using aerodynamic methods has thus far been demonstrated through constellation maintenance using differential drag [37,38] and proposed concepts exploiting differential lift [39]. Targeting of atmospheric re-entry location by drag augmentation [40] and adjustment of orbital inclination using out-of-plane forces [12] have also been studied. Passive aerodynamic stabilisation (aerostability), the pointing of a spacecraft in the direction of the oncoming flow, has been demonstrated in orbit by several missions [41–43], whilst further aerodynamic attitude concepts including detumbling [44] and pointing control [45–48] have also been considered.

The magnitude of the aerodynamic force (and torque by association) can be described by the following equation where ρ is the atmospheric flow density, V the relative flow velocity, S a reference area, and

C_F a corresponding force coefficient which is determined by the interaction between the flow and the surface [49].

$$F = \frac{1}{2}\rho V^2 S C_F$$

The forces experienced in orbit therefore increase with decreasing orbital altitude as the atmospheric density increases. A further contribution is also provided by the small increase in orbital velocity as altitude decreases. Using the NRLMSISE-00 atmosphere model with nominal input parameters, the increase in aerodynamic force with altitude, assuming a circular orbit, is shown in Figure 14. The reduction in orbital altitude from 600km to 300km for example is shown to increase the generated force over 200-fold and can therefore result in significantly increased effectiveness or efficiency of aerodynamic attitude and orbit control methods.

Aerostability, for example, has been shown to be possible up to an altitude of approximately 500km, with optimal results demonstrated for altitudes below 450km [50–52]. This is due to the dependence of aerodynamic stiffness on the residual atmospheric density and the relative magnitude of other perturbing torques, for example due to solar radiation pressure, residual magnetic dipoles, and gravity gradient.

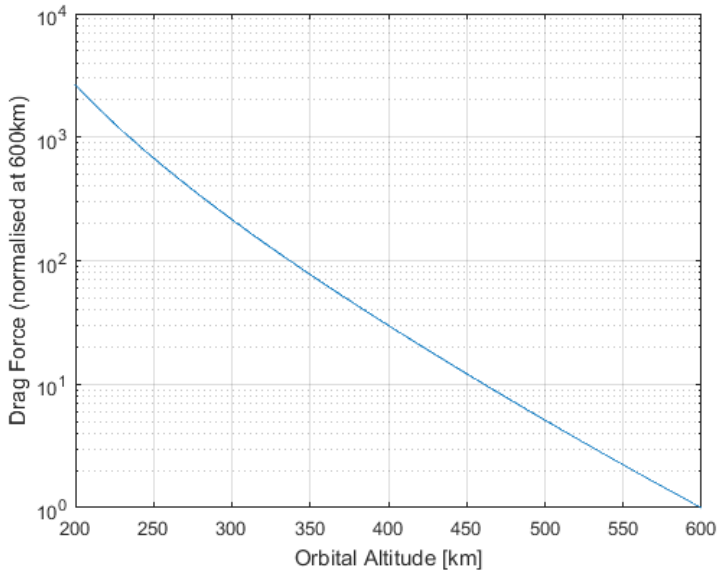

Figure 14 *Variation in drag force with altitude on a nominal surface in a circular orbit.*

A key consideration in the use of these forces is the ratio between lift (or out-of-plane force) and the drag force. As a result of the rarefied flow environment in LEO and the diffuse gas-surface interactions for typical spacecraft surface materials, this ratio is generally very low, on the order of 0.1 [12,53]. To utilise aerodynamic forces for control and manoeuvring purposes whilst also maintaining a reasonable orbital lifetime this ratio must therefore be increased through identification of new materials. Alternatively or additionally, some form of propulsion system is required to mitigate or counteract the effect of drag.

2.1.12. Atmosphere-Breathing Propulsion

The increased atmospheric density with decreasing orbital altitude also provides the opportunity to explore atmosphere-breathing propulsion systems [54]. Whilst electric propulsion systems are used widely for spacecraft propulsion due to their high specific impulse and therefore efficiency with respect to propellant use, the mass of propellant which can be carried by the spacecraft without depreciating other subsystems still limits the lifetime of the mission.

Atmosphere-Breathing Electric Propulsion (ABEP) systems on the other hand, shown in Figure 15, proposes to collect the oncoming atmospheric gas flow and to use this as the propellant for an electric thruster. Using this principle, the lifetime of the spacecraft can be significantly extended beyond current designs as the need for on-board propellant storage eliminated.

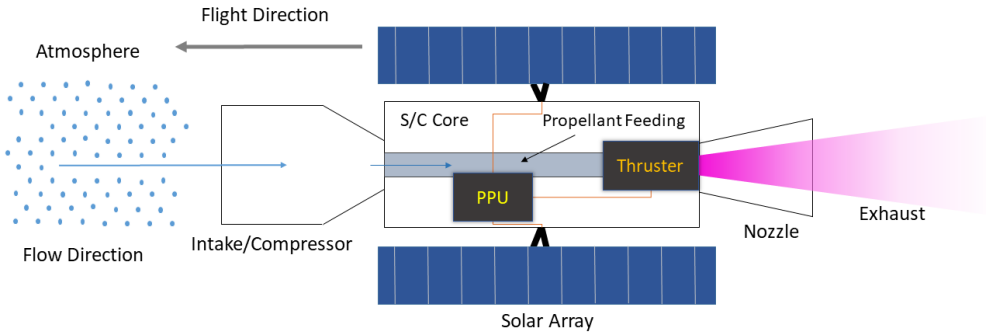

Figure 15 Generalised concept of Atmosphere-Breathing Electric Propulsion (ABEP) systems [RD-3].

The removal of propellant storage offers the opportunity to reduce the spacecraft mass and therefore the launch mass. However, this is dependent on the mass and efficiency of the atmospheric intake/compressor unit, thruster assembly, and any additional power-raising systems which are required, for example additional deployable solar arrays.

However, the drag contribution of these additional components also requires consideration as the corresponding thrust requirement may also increase significantly. Furthermore, the efficiency of atmospheric intakes is also expected to reduce with increasing mass flow rate [RD-3], therefore increasing system mass and drag contribution with reducing altitude. An optimal altitude range for ABEP propulsion therefore exists for given system performance, above which the atmospheric drag is low enough to allow conventional electric propulsion to provide a reasonable lifetime, and below which the additional mass of the system components becomes prohibitive.

A comprehensive review of current ABEP system concepts, rarefied atmospheric intake design, and electric thruster development, is provided in the DISCOVERER D4.1 Literature Review of ABEP Systems [RD-3].

2.2. Applications of Very Low Earth Orbit

This section links the previously described benefits to different Earth Observation system types and concepts, including those identified in the DISCOVERER D2.1 VLEO Aerodynamics Requirements [RD-1] and D5.1 Market Overview [RD-2] reports. The systems types are first categorised as either passive or active depending on the sensors used. Passive systems include optical, infrared, and radar, whilst active systems are classified as real aperture radar, Synthetic Aperture Radar (SAR), or LiDAR.

2.2.1. Passive Systems

2.2.1.1. Optical Systems

Optical systems can be generally classified into three primary categories:

- Panchromatic: imagery sensitive to a broad range of wavelengths of visible light, generally represented in black and white or greyscale.
- Multispectral: imaging in a small number of discrete spectral bands (small ranges of wavelengths). At minimum, the visible spectrum of red, green, and blue light is represented, but depending on the application many bands can be can captured including infrared and ultraviolet spectra.
- Hyperspectral: imagery is collected in many (hundreds) of narrow and contiguous spectral bands.

For a nadir-pointing telescope, the relationship between diffraction limited resolution and altitude for different wavelengths of light and a fixed lens diameter (1m) is given by Figure 16, demonstrating that the improvement in diffraction limited resolution with reducing altitude. Using the same relationship, the aperture diameter can similarly be reduced by lowering the orbital altitude, demonstrating a benefit in payload sizing which can be achieved whilst maintaining the same diffraction limited resolution.

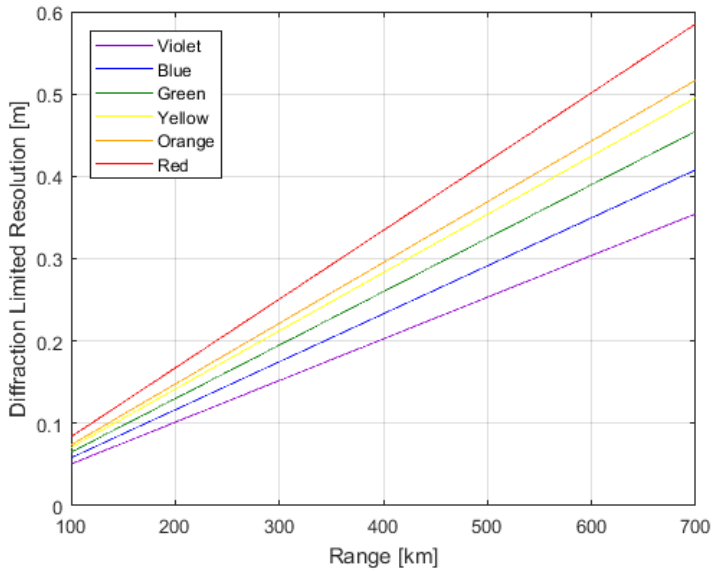

Figure 16 *Relationship between altitude/range and diffraction limited ground resolution for visible light of different wavelengths (for an aperture diameter of 1m).*

As the altitude of the spacecraft is reduced, the total footprint area available to the spacecraft for a given angular field of regard will decrease as demonstrated in Figure 17. As a result of the longer distance to the edge of the available footprint area, the resolution achievable with increasing field of regard will also decrease. The effect of this is greater at higher-altitudes, demonstrated in Figure 18.

If high off-nadir pointing performance is considered the resolution performance can vary significantly across the footprint. The elevation angle ε at the edge of the sensor footprint should also be considered as features at the target may become highly distorted or obscured at low angles of elevation.

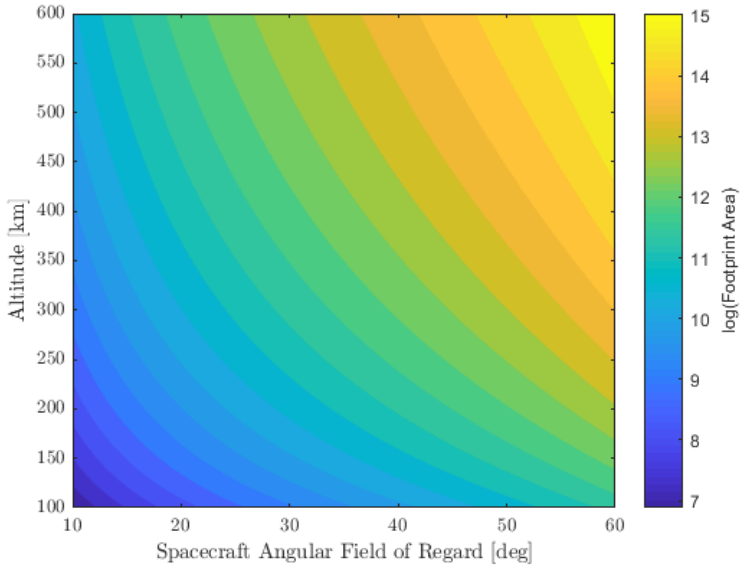

Figure 17 *Variation in footprint area with spacecraft angular field of regard and altitude for light at 700nm wavelength.*

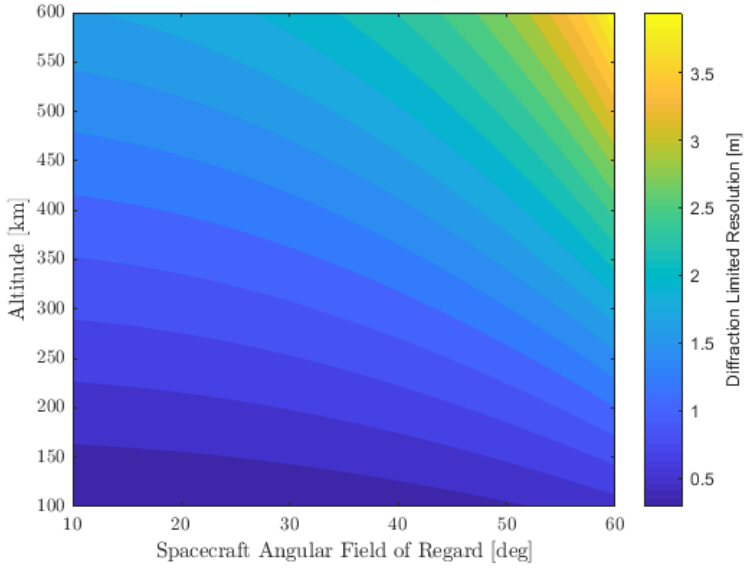

Figure 18 *Variation in diffraction limited resolution with spacecraft off-nadir pointing angle and altitude for light at 700nm wavelength.*

Whilst none of the principal contributing factors to the total MTF of an optical system demonstrate primary dependence on orbital altitude, several secondary effects or system trade-offs are apparent.

- MTF is improved by larger optical apertures or shorter focal length and therefore the payload design and specification.
- Whilst the atmospheric contribution to MTF is not directly related to orbital altitude, the range through the lower atmosphere which an image is acquired can affect the quality and will therefore vary with the off-nadir pointing angle utilized by the system.

MTF contributions from platform vibrations can be significantly influenced by the structural design and environmental factors. Density fluctuations, thermospheric wind effects, and the associated aerodynamic interactions may therefore influence this contribution to the MTF and will vary with the operational altitude and environmental conditions.

With regards to radiometric performance for optical based systems, a reduction in altitude will either enable smaller diameter apertures to be used whilst maintaining a given SNR. Alternatively, for a given sensor and aperture the dynamic range can be increased and SNR improved.

The benefits in spatial and radiometric performance with reducing altitude are particularly pertinent for hyperspectral instruments which are typically radiometrically and therefore also spatially constrained due to the narrow width of the individual imaging bands and therefore low SNR [55].

Low-cost panchromatic and multispectral optical imaging platforms for both coverage and high-resolution applications will also benefit from lower available orbital altitudes as the spatial resolution and SNR can be improved or smaller diameter optical apertures utilised, thus reducing mass and integration requirements.

2.2.1.2. Passive Infrared and Radar

Passive infrared and radar (radiometer) payloads sense either reflected or emitted radiation from the Earth. Applications for Earth orbiting systems include thermal infrared observation, microwave imaging, and GNSS reflectometry (principally for sea-state and windspeed monitoring).

Like optical observations, these methods are passive and therefore similarly benefit from reduction in the orbital altitude through improved spatial resolution and radiometric performance.

2.2.2. Active Systems

2.2.2.1. Real-Aperture Radar

Real aperture radar or Side-Looking Airborne Radar (SLAR) devices can be used for altimetry or scatterometer applications and offer the ability to penetrate cloud cover or distinguish objects by surface texture or roughness.

These devices are also constrained by the Rayleigh criterion. However, because of the longer-wavelength of radio waves, radar naturally has a larger diffraction limited resolution.

$$S_R \approx 1.22 \frac{\lambda R}{D}$$

The angular (ambiguity) resolution of radar S_a can also be expressed using the half-power (-3 dB) beamwidth angle Θ at the range R, describing the range at which two equally distant targets can be distinguished from each other [56].

$$S_a = 2R \sin \frac{\Theta}{2}$$

The range (ambiguity) resolution S_r of a radar describes the minimum linear distance between two targets along the same path from the antenna at which they can be distinguished from each other. For a pulse (rectangular step) waveform, this can be determined from the pulse-width τ and the speed of light c_0 [56].

$$S_r = \frac{c_0 \tau}{2}$$

The angular resolution of a real aperture radar system is improved by reducing the range to the target and can therefore be improved with a reduction in altitude. However, the range resolution is independent of the distance to the target. The combination of the angular and range resolution can be used to define a resolution cell which describes the spacing required to distinguish between multiple targets.

As an example, the nadir ground resolution of a 5cm wavelength radar with a 1m aperture diameter and at an orbital altitude of 300km is 18.3km. This demonstrates the limited use of real aperture radar for detection of ground-based features. However, for applications such as altimetry and ocean/wave-height measurement, the range resolution (vis. height) can be improved by pulse compression methods to provide useful outputs.

Due to the active component of a radar, the radiometric performance of these systems differs significantly from optical systems. The radar principle is based on the directed transmission of electromagnetic waves, backscattering by different surfaces and materials, and subsequent collection of the returned signal.

The P_r received signal power can be related to the and transmitted signal power P_t and receiving and transmitting antenna gains G_r and G_t. The distance (range) to the reflecting target is given by R, and the backscattering or radar cross-section by σ [57].

$$P_r = \frac{P_t G_t G_r \lambda^2 \sigma}{(4\pi)^3 R^4}$$

As the signal for an active radar system must travel both the distance to and back from the target, these systems can significantly benefit from any reduction in altitude, illustrated by the relationship of received power to the inverse of the fourth power of the range to the target. Consequently, the transmitting power required for such a system at a lower altitude can be significantly decreased whilst maintaining a similar signal to noise ratio.

The radiometric resolution for a radar is given by the ability of the detector to distinguish between targets with similar backscatter coefficient against the signal intensity and image speckle. An expression for the radiometric resolution can be given considering the average backscatter coefficient σ_0 and the associated standard deviation σ_p [58].

$$S_{rd} = 10 \log_{10} \left(1 + \frac{\sigma_p}{\sigma_0}\right)$$

Noise sources which contribute to degradation in the radiometric resolution include speckle noise resulting from the interference between backscattered waves, background thermal noise, noise internal to the sensor, and quantisation (analogue-to-digital conversion).

The SNR at the receiver for a real aperture radar can be expressed using the radar equation and utilising the following parameters: Boltzmann's constant k; the effective noise temperature T_e; the receiver noise bandwidth B_n; and the receiver noise factor (or ratio between input and output SNR) $\overline{NF}$ [59].

$$SNR = \frac{P_t G_t G_r \lambda^2 \sigma}{(4\pi)^3 k T_e B_n \overline{NF} R^4}$$

The result of this expression corresponds to the relationship between range and received power and demonstrates an improvement in SNR with the inverse of the fourth power of range with decreasing altitude. Alternatively, the SNR or transmitter power requirement for a monostatic radar can be shown to be improved with the square of the antenna area.

$$SNR = \frac{P_t \eta^2 A_r^2 \sigma}{4\pi k T_e B_n \overline{NF} R^4}$$

2.2.2.2. Synthetic Aperture Radar

Synthetic Aperture Radar (SAR) is an implementation of radar which allows for significantly improved resolution in the velocity direction of a spacecraft. A SAR payload is a typically side-facing radar which detects both the amplitude and phase of backscattered signal.

In contrast to real aperture radar, SAR takes advantage of the motion of the vehicle and observes targets over the total duration that they fall within the radar beamwidth. As the vehicle has moved over this period a larger aperture is synthesised and a higher resolution can be achieved. The length of this synthetic aperture length can be calculated by considering the platform along-track velocity V, illumination time T_e, and azimuth pointing angle θ_{Az}.

$$l_e = V T_e \sin \theta_{Az}$$

For the simplest case, a side-looking SAR sensor (indicated in Figure 19), where $\theta_{Az} = 90°$, the maximum azimuth (along-track) resolution of a SAR antenna can be defined as function of only the antenna length in that direction L_{Az} [58].

$$S_{Az} \geq \frac{L_{Az}}{2}$$

The azimuth, or in-track resolution of SAR is therefore independent of the wavelength, velocity, and range and proportional to the antenna length. Contrastingly to a real aperture radar, and somewhat counterintuitively, the along-track resolution of SAR improves as the antenna size is reduced (though the signal to noise ratio is reduced).

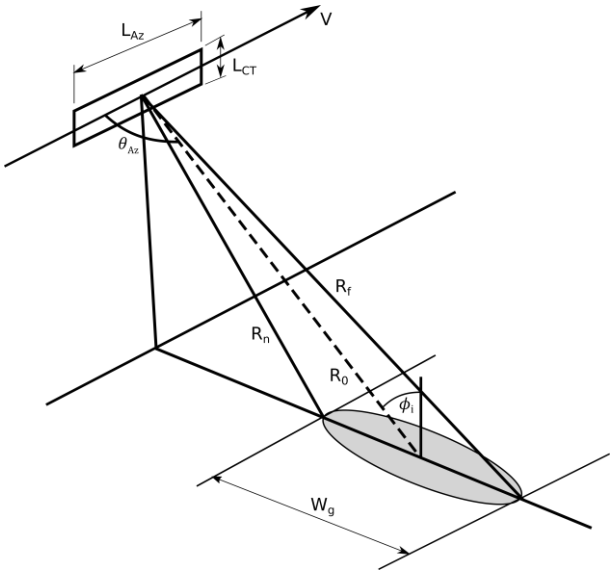

Figure 19 *SAR footprint geometry. Adapted from Wertz et al.* [60].

Similar to the range resolution of a traditional radar, the cross-track (range) resolution of SAR is dependent on the speed of light c_0, pulse-width τ, and for a side-facing antenna can be defined using the slant-angle to the target ϕ_i.

$$S_{CT} = \frac{c_0 \tau}{2 \sin \phi_i}$$

The cross-track resolution of SAR can therefore be improved by increasing the off-nadir viewing angle and has a theoretical maximum at 90°.

The antenna height is dependent on the wavelength, swath width, range, and incidence, and therefore affects the area of ground which can be covered by the SAR in a pass.

$$L_{CT} = \frac{\lambda R_0}{w_g \cos \phi_i}$$

The minimum antenna area can be seen to increase for greater velocity, wavelength, range, and incidence angle. The sizing of a SAR antenna will therefore benefit from a reduction in orbit altitude for the same angle of incidence. However, SAR is still subject to ambiguity constraints based on the frequency of the transmitted pulse, or pulse repetition frequency (PRF). In the along-track direction, the PRF $(1/\tau)$ is limited by the velocity and antenna length, such that the vehicle only translates half the length of the antenna during each pulse (azimuth ambiguity) [61].

$$PRF_{min} = \frac{1}{\tau_{min}} > \frac{2V}{L_{Az}}$$

Similarly, to avoid detection of multiple echoes in the cross-track direction (range ambiguity), a maximum PRF is defined based on the range to near R_n and far R_f sides of the sensor footprint.

$$PRF_{max} < \frac{1}{2\tau_{max} + 2(R_f - R_n)c^{-1}}$$

As the ambiguity constraints on PRF are based on geometric considerations of the antenna, a minimum antenna area can be determined.

$$A_{min} = L_{Az} L_{CT} = \frac{PRF_{max}}{PRF_{min}} \frac{4V\lambda R_0}{c} \tan \phi_i$$

The SNR of a SAR payload is given by Tomiyasu [61] and Cutrona [62].

$$SNR = \frac{P_{av} A_r^2 \eta^2 S_{CT} \sigma}{8\pi k T_r R_0^3 \overline{NF} V \lambda L_s}$$

where η is an antenna efficiency factor, σ is the radar cross-section, T_r is the receiver absolute temperature, $\overline{NF}$ is a relative noise factor, and L_s is the total system loss. The SNR is reduced with

wavelength, platform velocity, and the cube of the target range. This contrasts with conventional radar which reduces with the fourth-power of the target range. This improvement results from the integration of a number of pulses during the generation of the synthetic aperture. The SNR also improves for a greater (worse) resolution in the cross-track direction but is independent of the azimuth resolution. If the minimum antenna area is considered (proportional to the range), the SNR relationship with range is also reduced to a linear function for a SAR payload. A reduction in orbit altitude whilst maintaining the minimum antenna area will therefore only improve the power requirement linearly.

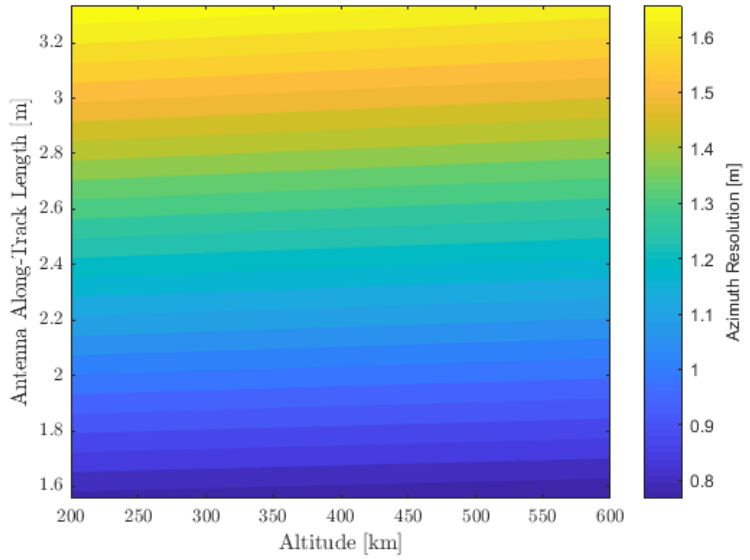

Figure 20 *Relationship between SAR along-track antenna length and azimuth resolution for varying altitude, a swath width of 30km, and viewing angle of 45 deg*

Parametric relationships between power, resolution, antenna area, and SNR are illustrated in Figure 20, 21 and 22. The general independence of SAR resolution with altitude and inverse relationship with along-track antenna length is demonstrated in Figure 20, demonstrating that the azimuth resolution in fact benefits from a smaller physical along-track antenna length.

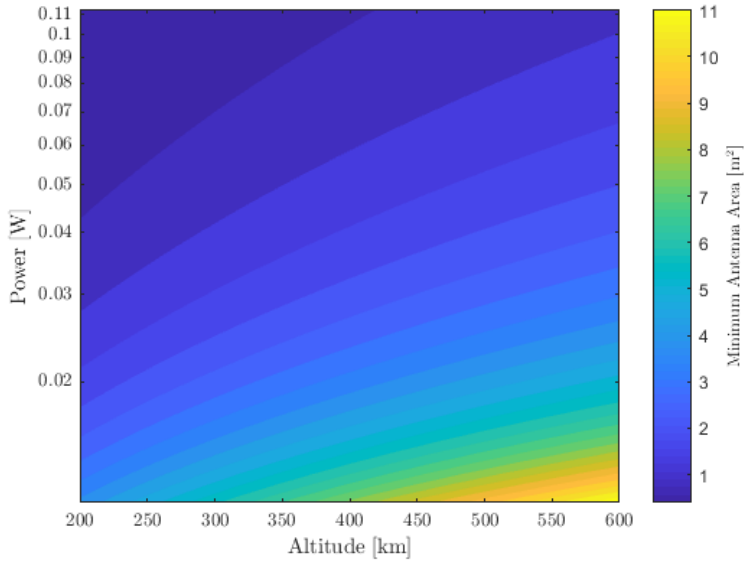

Figure 21 *Relationship between SAR power requirement and minimum antenna area for a SNR of three for varying orbital altitude, a swath width of 30km, and viewing angle of 45 deg. A PRF ratio of 1.2 is used for reference.*

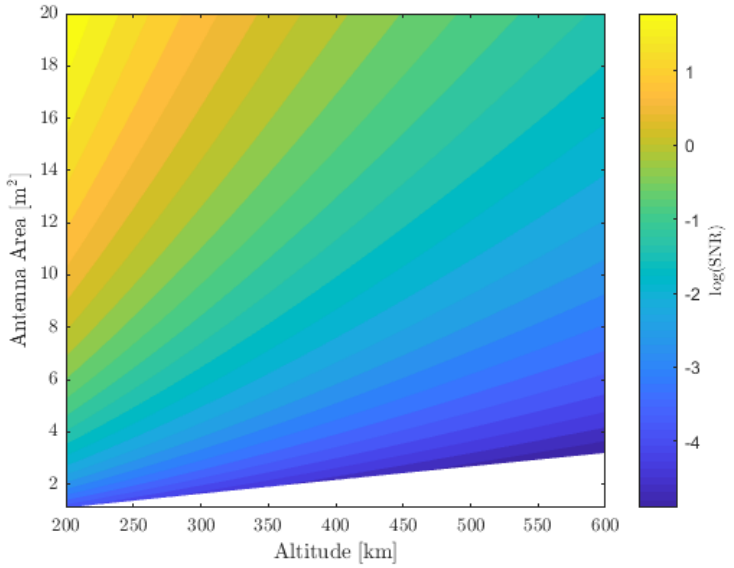

Figure 22 *Relationship between SAR antenna area and SNR for varying orbital altitude, a swath width of 30km, and viewing angle of 45 deg. A fixed power of 5mW is used for reference. Note the log-scale for SNR.*

The relationship between altitude (for a given off-axis viewing angle), minimum antenna area, and power is shown in Figure 21. In this case, the antenna size is maintained at the minimum required for a given SNR and the required power calculated. Figure 21 demonstrates the benefit in transmitter power requirement which can be achieved through a reduction in orbiting altitude. However, the minimum antenna area is also shown to be necessary if the power is reduced.

Figure 22 indicates the relationship between antenna area (from minimum area) and signal-to-noise (SNR) ratio for a fixed power input. This relationship demonstrates that an increased antenna area and reduced orbital altitude result in an improved SNR.

2.2.2.3. LiDAR

LiDAR sensors have also recently been used on spacecraft for generation of digital elevation models and terrain mapping activities. The range resolution or vertical accuracy of a LiDAR sensor is not dependent on the altitude, but on the available resolution of the available clock or timing measurement chain. The range of LiDAR is however dependent on the reflected signal strength, and ambient noise factors. A reduction in altitude or range to target will therefore improve SNR or allow a lower power laser pulse.

As with active radar, the returned power of the signal will improve by a power of four with a shorter range to the target. This returned power is also dependent on the beam divergence β, atmospheric and system transmission factors η, and the target backscatter coefficient σ [63].

$$P_r = \frac{P_t \eta_{atm} \eta_{sys} D_r^2 \sigma}{4\pi R^4 \beta^2}$$

The beam divergence of LiDAR can be calculated using the Rayleigh criterion (see Section 2.1.1). The projected footprint area is then dependent on the wavelength, aperture size, and the range to the target/ground and defines the minimum feature size which can be observed [64,65]. In comparison to radar, the significantly shorter (typically near-infrared) wavelengths used in LiDAR result in much smaller ground footprints and can therefore achieve a higher linear resolution.

In a line scanning mode the measurement spacing or spatial resolution S_L of LiDAR is dependent on the pulse repetition frequency (PRF) and the ground velocity [66].

$$S_L = \frac{V_g}{PRF}$$

As the altitude is lowered, the orbital velocity will increase, and the spatial resolution due to the pulse frequency will decrease for the same PRF and may becoming limiting.

3. References

[1] J. Virgili Llop, P.C.E. Roberts, Z. Hao, L. Ramio Tomas, V. Beauplet, Very Low Earth Orbit mission concepts for Earth Observation: Benefits and challenges, in: 12th Reinventing Sp. Conf., London, UK, 2014: pp. 1–18.

[2] J.R. Schott, Remote Sensing: The Image Chain Approach, 2nd ed., Oxford University Press Inc., New York, NY, 2007. doi:10.5860/CHOICE.35-4512.

[3] D.A. Vallado, Fundamentals of Astrodynamics and Applications, 4th ed., Microcosm Press/Springer, Hawthorne, CA, 2013.

[4] N. Koren, Understanding Image Sharpness Part 1: Introduction to Resolution and MTF Curves, (n.d.). http://www.normankoren.com/Tutorials/MTF.html (accessed July 23, 2018).

[5] G.D. Boreman, Transfer Function Techniques, in: Handb. Opt., 2nd ed., McGraw-Hill, New York, NY, 1995.

[6] D. Sadot, S. Shamriz, I. Dror, N.S. Kopeika, Prediction of overall atmospheric modulation transfer function with standard weather parameters: comparison with measurements with two imaging systems, Opt. Eng. 34 (1995) 3239–3248. doi:10.1117/12.213657.

[7] D. Sadot, N.S. Kopeika, Imaging through the atmosphere: practical instrumentation-based theory and verification of aerosol modulation transfer function, J. Opt. Soc. Am. A. 10 (1993) 172. doi:10.1364/JOSAA.10.000172.

[8] D. Wulich, N.S. Kopeika, Image resolution limits resulting from mechanical vibrations, Opt. Eng. 26 (1987).

[9] J. Haghshenas, Vibration effects on remote sensing satellite images, Adv. Aircr. Spacecr. Sci. 4 (2017) 543–553. doi:10.12989/aas.2017.4.5.543.

[10] J.F. Silny, L. Zellinger, Radiometric sensitivity contrast metrics for hyperspectral remote sensors, in: SPIE Opt. Eng. + Appl., SPIE, San Diego, CA, 2014. doi:10.1117/12.2063511.

[11] A.J.E. Smith, A practical method for computing SAR satellite revisit times: application to RADARSAT-1 and ENVISAT, Int. J. Remote Sens. 28 (2007) 1123–1135. doi:10.1080/01431160500307094.

[12] J. Virgili Llop, P.C.E. Roberts, K. Palmer, S.E. Hobbs, J. Kingston, Descending Sun-Synchronous Orbits with Aerodynamic Inclination Correction, J. Guid. Control. Dyn. 38 (2015) 831–842. doi:10.2514/1.G000183.

[13] J.R. Wertz, W.J. Larson, eds., Space Mission Analysis and Design, 3rd ed., Microcosm Press/Kluwer Academic Publishers, El Segundo, CA, 1999.

[14] J. van den IJssel, P. Visser, E. Doornbos, U. Meyer, H. Bock, A. Jäggi, GOCE SSTI L2 Tracking Losses and their Impact on POD Performance, in: 4th Internatonal GOCE User Work., European Space Agency (ESA), Munich, 2011.

[15] L.J. Ippolito, Radiowave Propagation in Satellite Communications, Springer Netherlands, Dordrecht, 1986. doi:10.1007/978-94-011-7027-7.

[16] P. Fortescue, G. Swinerd, J. Stark, eds., Spacecraft Systems Engineering, 4th ed., John Wiley & Sons, Ltd., Chichester, UK, 2011.

[17] Inter-Acency Space Debris Coordination Committee: Steering Group and Working Group 4, IADC Space Debris Mitigation Guidelines, 2007.

[18] J.J.F. Liu, R.L. Alford, Semianalytic Theory for a Close-Earth Artificial Satellite, J. Guid. Control. Dyn. 3 (1980) 304–311. doi:10.2514/3.55994.

[19] J.M. Picone, A.E. Hedin, D.P. Drob, A.C. Aikin, NRLMSISE-00 Empirical Model of the Atmosphere: Statistical Comparisons and Scientific Issues, J. Geophys. Res. 107 (2002). doi:10.1029/2002JA009430.

[20] D.L. Oltrogge, C.-C. Chao, Standardized Approaches for Estimating Orbital Lifetime after End-of-Life, in: AIAA/AAS Astrodyn. Spec. Conf., American Astronautical Society (AAS), Mackinac Island, MI, 2007.

[21] H. Klinkrad, Space Debris: Models and Risk Analysis, Springer-Science+Business Media, 2006.

[22] S. Flegel, MASTER-2009 Software User Manual, 2011.

[23] Scientific and Technical Subcommittee of the United Nations Committee on the Peaceful uses of Outer Space, Technical Report on Space Debris, New York, NY, 1999.

[24] E.G. Stassinopoulos, J.P. Raymond, The space radiation environment for electronics, Proc. IEEE. 76 (1988) 1423–1442. doi:10.1109/5.90113.

[25] M.M. Finckenor, K.K. de Groh, Space Environmental Effects, National Aeronautics and Space Administration (NASA), 2015.

[26] D. Heynderickx, B. Quaghebeur, E. Speelman, E. Daly, ESA's Space Environment Information System (SPENVIS) - A WWW interface to models of the space environment and its effects, in: 38th Aerosp. Sci. Meet. Exhib., American Institute of Aeronautics and Astronautics (AIAA), Reno, NV, 2000. doi:10.2514/6.2000-371.

[27] G.D. Badhwar, The radiation environment in low-Earth orbit., Radiat. Res. 148 (1997) S3–S10. doi:10.2307/3579710.

[28] C.R. Boshuizen, J. Mason, P. Klupar, S. Spanhake, Results from the Planet Labs Flock Constellation, in: 28th Annu. AIAA/USU Conf. Small Satell., American Institute of Aeronautics and Astronautics (AIAA), Logan, UT, 2014.

[29] G. Tyc, J. Tulip, D. Schulten, M. Krischke, M. Oxfort, The RapidEye Mission Design, in: Acta Astronaut., 2005: pp. 213–219. doi:10.1016/j.actaastro.2004.09.029.

[30] C. Underwood, G. Richardson, J. Savignol, SNAP-1: A Low Cost Modular COTS-Based Nano-Satellite - Design, Construction, Launch and Early Operations Phase, in: 15th Annu. AIAA/USU Conf. Small Satell., American Institute of Aeronautics and Astronautics (AIAA), Logan, UT, 2001: pp. 1–7.

[31] M.N. Sweeting, Modern Small Satellites - Changing the Economics of Space, Proc. IEEE. 106 (2018) 343–361. doi:10.1109/JPROC.2018.2806218.

[32] Space Exploration Technologies, Falcon 9 Launch Vehicle Payload User's Guide Rev2, Hawthorne, CA, 2015.

[33] Rocket Lab USA, Payload User's Guide 4.0, Huntington Beach, CA, 2016.

[34] Orbital Sciences Corporation, Pegasus User's Guide 8.0, Dulles, VA, 2015.

[35] Arianespace, Vega User's Manual Issue 4 Revision 0, Évry-Courcouronnes, France, 2014.

[36] Orbital Sciences Corporation, Antares OSP-3 User's Guide Release 1.1, Dulles, VA, 2013.

[37] C. Foster, H. Hallam, J. Mason, Orbit determination and differential-drag control of Planet Labs cubesat constellations, Adv. Astronaut. Sci. 156 (2016) 645–657.

[38] J.W. Gangestad, B.S. Hardy, D.A. Hinkley, Operations, Orbit Determination, and Formation Control of the AeroCube-4 CubeSats, in: 27th Annu. AIAA/USU Conf. Small Satell., American Institute of Aeronautics and Astronautics (AIAA), Logan, UT, 2013.

[39] M. Horsley, S. Nikolaev, A. Pertica, Small Satellite Rendezvous Using Differential Lift and Drag, J. Guid. Control. Dyn. 36 (2013) 445–453. doi:10.2514/1.57327.

[40] J. Virgili Llop, P.C.E. Roberts, N.C. Hara, Atmospheric Interface Reentry Point Targeting Using Aerodynamic Drag Control, J. Guid. Control. Dyn. 38 (2015) 403–413. doi:10.2514/1.G000884.

[41] R.R. Kumar, D.D. Mazanek, M.L. Heck, Simulation and Shuttle Hitchhiker validation of passive satellite aerostabilization, J. Spacecr. Rockets. 32 (1995) 806–811. doi:10.2514/3.26688.

[42] M.R. Drinkwater, R. Haagmans, D. Muzi, A. Popescu, R. Floberghagen, M. Kern, M. Fehringer, The GOCE Gravity Mission: ESA'S First Core Earth Explorer, in: 3rd Int. GOCE User Work., European Space Agency (ESA), Frascati, Italy, 2007: pp. 1–7. doi:ISBN 92-9092-938-3.

[43] V.A. Sarychev, S.A. Mirer, A.A. Degtyarev, E.K. Duarte, Investigation of equilibria of a satellite subjected to gravitational and aerodynamic torques, Celest. Mech. Dyn. Astron. 97 (2007) 267–287. doi:10.1007/s10569-006-9064-3.

[44] Z. Hao, P.C.E. Roberts, Using Aerodynamic Torques To Aid Detumbling Into an Aerostable State, in: 67th Int. Astronaut. Congr., International Astronautical Federation (IAF), Guadalajara, Mexico, 2016.

[45] M.L. Gargasz, Optimal Spacecraft Attitude Control Using Aerodynamic Torques, Air Force Institute of Technology, 2007.

[46] J. Virgili Llop, P.C.E. Roberts, Z. Hao, Aerodynamic Attitude and Orbit Control Capabilities of The ΔDsat CubeSat, in: 37th Annu. AAS Guid. Control Conf., American Astronautical Society (AAS), Breckenridge, CO, 2014.

[47] J. Auret, W.H. Steyn, Design of an Aerodynamic Attitude Control System for a Cubesat, 62nd Int. Astronaut. Congr. (2011).

[48] Y.H. Chen, Z.C. Hong, C.H. Lin, J.S. Chern, Aerodynamic and gravity gradient stabilization for microsatellites, Acta Astronaut. 46 (2000) 491–499. doi:10.1016/S0094-5765(99)00191-5.

[49] NASA, Spacecraft Aerodynamic Torques, 1971.

[50] M.L. Psiaki, Nanosatellite Attitude Stabilization Using Passive Aerodynamics and Active Magnetic Torquing, J. Guid. Control. Dyn. 27 (2004) 347–355. doi:10.2514/1.1993.

[51] S.A. Rawashdeh, J.E. Lumpp, Aerodynamic Stability for CubeSats at ISS Orbit, J. Small Satell. 2 (2013) 85–104.

[52] J. Armstrong, C. Casey, G. Creamer, G. Dutchover, Pointing Control for Low Altitude Triple Cubesat Space Darts, in: 23rd Annu. AIAA/USU Conf. Small Satell., American Institute of Aeronautics and Astronautics (AIAA), Logan, UT, 2009: pp. 1–8.

[53] D.G. King-Hele, Satellite Orbits in an Atmosphere: Theory and Applications, Blackie and Son Ltd., Glasgow, UK, 1987.

[54] T. Schönherr, K. Komurasaki, F. Romano, B. Massuti-Ballester, G. Herdrich, Analysis of atmosphere-breathing electric propulsion, IEEE Trans. Plasma Sci. 43 (2015) 287–294. doi:10.1109/TPS.2014.2364053.

[55] J. Transon, R. D'Andrimont, A. Maugnard, P. Defourny, Survey of Hyperspectral Earth Observation Applications from Space in the Sentinel-2 Context, Remote Sens. 10 (2018) 157. doi:10.3390/rs10020157.

[56] Radar Systems Panel IEEE Aerospace and Electronic Systems Society, IEEE Standard for Radar Definitions, in: IEEE Std 686-2017 (Revision IEEE Std 686-2008), 2017. doi:10.1109/IEEESTD.2017.8048479.

[57] H.R. Raemer, Radar Systems Principles, CRC Press, Boca Raton, FL, 1997.

[58] P. Lacomme, J.-P. Hardange, J.-C. Marchais, E. Normant, Air and Spaceborne Radar Systems, 2001. doi:10.1016/B978-189112113-5.50030-9.

[59] V. Jain, P. Heydari, Radar Fundamentals, in: Automot. Radar Sensors Silicon Technol., 1st ed., Springer-Verlag, New York, 2013: pp. 1–97. doi:10.1007/978-1-4419-6775-6.

[60] J.R. Wertz, D.F. Everett, J.J. Puschell, eds., Space Mission Engineering: The New SMAD, 1st ed., Microcosm Press, Hawthorne, CA, 2011.

[61] K. Tomiyasu, Tutorial Review of Synthetic-Aperture Radar (SAR) with Applications to Imaging of the Ocean Surface, Proc. IEEE. 66 (1978) 563–583. doi:10.1109/PROC.1978.10961.

[62] L.J. Cutrona, Synthetic Aperture Radar, in: M.I. Skolnik (Ed.), Radar Handb., 2nd ed., McGraw-Hill, New York, NY, 1990.

[63] A. Kashani, M. Olsen, C. Parrish, N. Wilson, A Review of LIDAR Radiometric Processing: From Ad Hoc Intensity Correction to Rigorous Radiometric Calibration, Sensors. 15 (2015) 28099–28128. doi:10.3390/s151128099.

[64] J.L. Bufton, Laser Altimetry Measurements from Aircraft and Spacecraft, Proc. IEEE. 77 (1989) 463–477. doi:10.1109/5.24131.

[65] J.N. Pelton, S. Madry, S. Camacho-Lara, eds., Handbook of Satellite Applications, Springer New York, New York, NY, 2013. doi:10.1007/978-1-4419-7671-0.

[66] X. Sun, Lidar Sensors From Space, in: S. Liang (Ed.), Compr. Remote Sens., Elsevier, 2018: pp. 412–434. doi:10.1016/B978-0-12-409548-9.10327-6.

4. Internal Reference Documents

Ref.	Document Title	Version, Date
RD-1	DISCOVERER-D2.1-VLEO Aerodynamic Requirements	1, 23/03/2018
RD-2	DISCOVERER-D5.1-EO Market Overview	11, 21/03/2018
RD-3	DISCOVERER-D4.1-Literature Review of ABEP Systems	1, 11/07/2017

5. Tables and other supporting documents where applicable and necessary

5.1. Acronyms and Abbreviations

EIRP	Effective Isentropic Radiated Power
EO	Earth Observation
GCP	Ground Control Point
GPS	Global Positioning System
GSD	Ground Sample Distance
IADC	Inter-Agency Space Debris Coordination Committee
LEO	Low Earth Orbit
MRT	Maximum Revisit Time
MTF	Modulation Transfer Function
PRF	Pulse Repetition Frequency
PSF	Point Spread Function
SAR	Synthetic Aperture Radar
SFU	Solar Flux Units
SNR	Signal to Noise Ratio
SSO	Sun Synchronous Orbit
VLEO	Very Low Earth Orbit

5.2. Nomenclature

A	Area
B_n	Noise bandwidth
D	Aperture diameter
E	Error
G	Antenna gain
L	Length
L_a	Transmission path loss
N	Noise
P	Power
R	Range
R_a	Atmospheric path length

R_ϕ	Earth radius at latitude
S	Signal
S_R	Resolution
T	Temperature
V	Velocity
c_0	Speed of light
f	Focal length
k	Boltzmann's constant
h_T	Target altitude
r_s	Satellite orbit radius (geocentric)
t	Time
Θ	Beamwidth angle
β	Beam divergence
x	Pixel size
σ	Radar cross-section (backscattering coefficient)
ϕ	Latitude
ϕ_i	Slant angle
η	Efficiency
θ	Ground range of field of regard
ψ	Angular field of regard
τ	Pulse-width
λ	Wavelength
ν	Spatial frequency
$\overline{NF}$	Noise factor
ℓ	Distance between pixel centres

6. Acknowledgements and Disclaimer

The DISCOVERER project has received funding from the European Union's Horizon 2020 research and innovation programme under grant agreement No 737183.